J Physiol 600.21 (2022) pp 4585–4601

REVIEW-SYMPOSIUM

Photoreceptor physiology and evolution: cellular and molecular basis of rod and cone phototransduction

Trevor D. Lamb

Eccles Institute of Neuroscience, John Curtin School of Medical Research, The Australian National University, Canberra, Australian Capital Territory, Australia

Edited by: Ian Forsythe & Omar Mahroo

The peer review history is available in the supporting information section of this article (https://doi.org/10.1113/JP282058#support-information-section).

Abstract The detection of light in the vertebrate retina utilizes a duplex system of closely related rod and cone photoreceptors: cones respond extremely rapidly, and operate at 'photopic' levels of illumination, from moonlight upwards; rods respond much more slowly, thereby obtaining greater sensitivity, and function effectively only at 'scotopic' levels of moonlight and lower. Rods and cones employ distinct isoforms of many of the proteins in the phototransduction cascade, and they thereby represent a unique evolutionary system, whereby the same process (the detection of light) uses a distinct set of genes in two classes of cell. The molecular mechanisms of phototransduction activation are described, and the classical quantitative predictions for the onset phase of the electrical response to light are developed. Recent work predicting the recovery phase of the rod's response to intense flashes is then presented, that provides an accurate account of the time that the response spends in saturation. Importantly, this also provides a new estimate for the rate at which a single rhodopsin activates molecules of the G-protein, transducin, that is substantially higher than other estimates in the literature. Finally, the evolutionary origin of the phototransduction proteins in rods and cones is examined, and it is shown that most of the rod/cone differences were established at the first of the two rounds of whole-genome duplication more than 500 million years ago.

(Received 6 December 2021; accepted after revision 29 March 2022; first published online 12 April 2022)
Corresponding author Trevor D. Lamb: John Curtin School of Medical Research, The Australian National University, Canberra, ACT 2601, Australia. Email: trevor.lamb@anu.edu.au

After undergraduate Electrical Engineering in Melbourne, **Trevor D. Lamb** moved to Cambridge in 1971 for his PhD in Physiology, and was mentored by Alan Hodgkin and Denis Baylor. Ever since that time his primary research interest has been in photoreceptors. A post-doc at Stanford with Denis and King-Wai Yau in 1977 led to the discovery of single-photon responses in rods. Trevor was Secretary of this *Journal*'s Editorial Board when it was decided in 1989 to abandon the alphabetical order of authors' names. After 31 years in Cambridge, Trevor returned to Australia in 2003 as a Federation Fellow at ANU; he is now Emeritus.

This review was presented at the Physiology 2021 symposium 'Photoreceptors in Health and Monogenic Disease: Advances in Understanding Physiology and Treating Pathophysiology' on 16 July 2021, organised by Dr Omar Mahroo, UCL Institute of Ophthalmology, UK.

DOI: 10.1113/JP282058

The Journal of Physiology

Introduction: rod and cone outer segment discs and sacs

In the triply immuno-labelled image of monkey retina in Fig. 1*A* (courtesy of Professor Nicolás Cuenca), seven cone photoreceptors are visible in their entirety, along with just the outer segments and synaptic terminals of the more numerous rods. The main anatomical features of rod and cone photoreceptor cells are portrayed schematically in Fig. 1*B* for the large photoreceptors typically found in cold-blooded species. The visual pigment (rhodopsin or a cone opsin) is incorporated at a very high spatial density (25,000 molecules μm^{-2}) in the lipid membrane of the 'outer segment'. This light-sensitive outer segment is a highly modified cilium, in which a huge amount of membrane has been synthesized.

Rods and cones differ in an important manner with respect to the topology of the pigment-containing membrane: in cones, the membranous 'sacs' are simply evaginations of the plasma membrane, whereas in rods a process of membrane fusion has taken place at the rim, so that the rod 'discs' comprise individual sealed-off compartments, as shown in the electron micrograph in Fig. 1*C* from Steinberg et al. (1980). Hence, in rods the intra-discal milieu has no contact with the extracellular solution, whereas in cones the corresponding milieu is the extracellular solution itself. For both rods and cones, the inter-disc (or inter-sac) spacing is ∼30 nm, meaning that there are roughly 30 discs or sacs per μm length of outer segment; consequently, a typical mammalian rod (with an outer segment length of 20−25 μm) would contain 700−800 discs.

The process of renewal of outer segment material is noteworthy. New membrane is continually synthesized at the base of the outer segment, in the vicinity of the ciliary neck; at the same time, newly synthesized rhodopsin (or cone opsin) is transported from the inner segment and incorporated into the new membrane. In both rods and cones, the newly synthesized membrane evaginates to form basal sacs, and a process of rim formation starts (Steinberg et al., 1980). However, it is only in rods that the process of rim formation proceeds around the entire circumference, to produce sealed-off discs. New discs are continually being formed beneath recently formed ones, with the result that the discs slowly migrate along the length of the outer segment. To avoid continual elongation of the rod outer segment, a process of phagocytosis occurs, whereby from time to time a chunk at the tip of the outer segment is 'chewed off' by the adjacent retinal pigment epithelium. The process of migration along the outer segment takes roughly 2−3 weeks in a mammalian rod. Why it occurs is not fully understood. But one possibility is to ensure the removal of 'old' rhodopsin (or other) molecules that have suffered weeks of photo-induced oxidative damage.

Photoresponse: mechanisms of activation and recovery

Activation: molecular interactions and predicted rising phase kinetics. The molecular interactions underlying the activation phase of the photoreceptor's response to light are indicated schematically in Fig. 2. The absorption of a photon isomerizes a single photopigment molecule (rhodopsin, or its cone equivalent), and that photoisomerization triggers activation of the photopigment to a configuration denoted R*. As a result of molecular contacts resulting from lateral diffusion, the single R* sequentially activates numerous molecules of the G-protein, transducin (G). The α-subunit of each activated transducin (Gα) is released, and through continued lateral diffusion it then partly activates a molecule of phosphodiesterase (PDE) by binding to one of its two inhibitory γ-subunits, thereby partly relieving the inhibition; for full activation of the PDE, both γ-subunits must have bound a molecule of Gα. The activated PDE hydrolyses the cytoplasmic messenger cyclic GMP (cG), and the resulting reduction in cytoplasmic cyclic GMP concentration causes closure of the cyclic nucleotide-gated ion channels (CNGCs). This reduces the influx of cations into the cell, making the interior more negative and thereby generating the photoreceptor's hyperpolarizing electrical response to light.

Note that the topology of the membrane in the depiction in Fig. 2 is a generic form representing both cone and rod phototransduction. For cones, which mediate photopic (daytime) vision, all of these proteins are located in the plasma membrane, as sketched. In contrast, for rods, which mediate scotopic (night-time) vision, only the ion channels and the sodium/calcium–potassium exchanger (NCKX; not shown in Fig. 2) are located in the plasma membrane. The other proteins are restricted almost exclusively in the membranes of the pinched-off free-floating discs, with the disc and plasma membranes being separated from each other by the cytoplasmic medium (see Fig. 1).

The activation phase of the phototransduction cascade was modelled quantitatively by Lamb and Pugh (1992), with the predictions sketched in Fig. 3, and that model still provides a good description of the onset phase of the rod's electrical response. The main simplifying assumption was to ignore all inactivation steps (rhodopsin shut-off, transducin/PDE shut-off, and elevated guanylyl cyclase activity), which restricted the validity of the predictions to relatively early times. In response to a brief flash of light that delivered a single photoisomerization at time zero, a single R* was activated, and (in the absence of shut-off) simply remained present, as shown by the step response for $R^*(t)$ in Fig. 3*A*. This R* then activated transducins at a constant rate, as shown in Fig. 3*B* by the green $G^*(t)$ straight-line trace, with slope ν_{G^*}. Analysis of diffusional

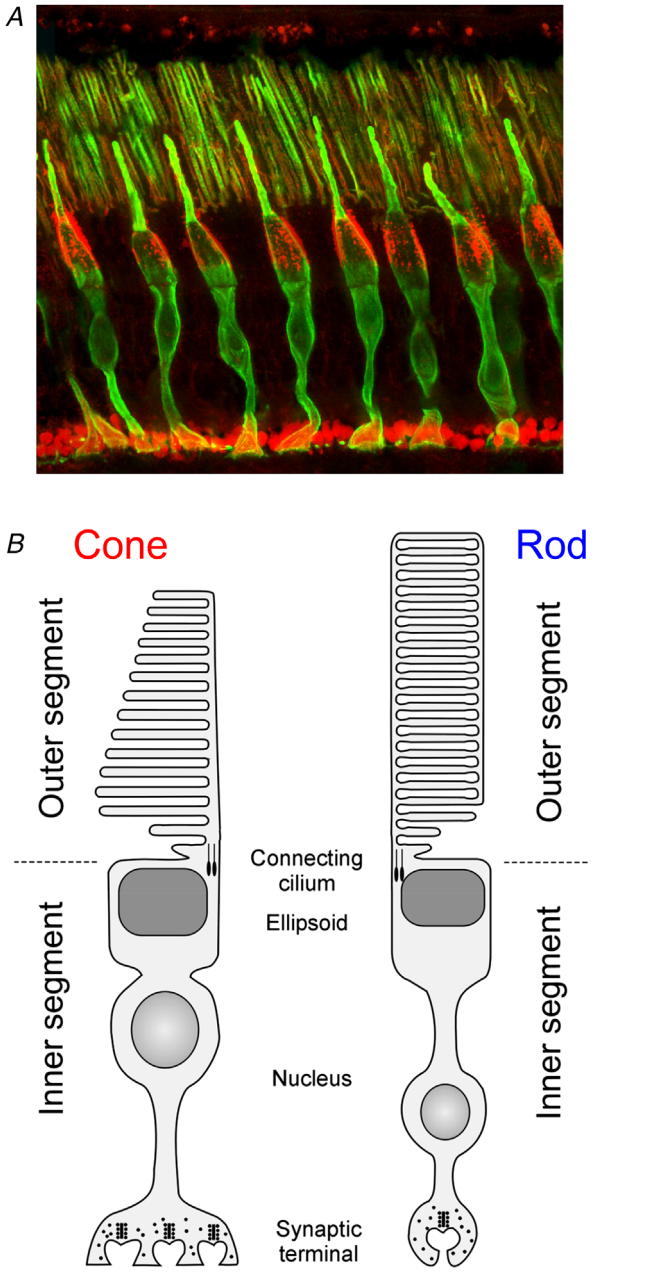

Figure 1. Retinal section, and cone and rod outer segments
A, retinal section, courtesy of Nicolás Cuenca, University of Alicante. The monkey retinal section was triple immuno-labelled with antibodies against α-synuclein (in red) and against arrestin and rhodopsin (both in green), to show the entire morphology of the cones (green, elongated cells) from the outer segment to the axon terminal (pedicle), together with just the outer segment (uppermost green lines) and axon terminal (spherule, red dots) of the more numerous rods. This image won first prize in the vision-research.eu picture competition 2009 (www.vision-research.eu/index.php?id=471). *B*, schematic diagrams of cone and rod photoreceptors. The light-sensitive outer segment is a modified cilium that extends from the cell's conventional inner segment, beyond a level termed the outer limiting membrane (indicated by the dashed line). Modified from Burns and Lamb (2003). *C*, electron micrograph of a region of rod outer segment from rhesus monkey shows a stack of discrete sealed-off discs that can be seen to be separate from the plasma membrane (pm); the diameter of this outer segment is ~2 μm. From Steinberg et al. (1980).

movement of proteins at the disc surface indicated that the coupling of transducin to PDE should be quite efficient, and so the number of activated PDE subunits is likewise predicted to ramp with time, as shown by the dashed blue $E^{*}(t)$ trace that has a somewhat lower slope; in terms of the activation of PDE holomers, the continuous blue trace for $E^{**}(t)$ has half this slope, $\nu_{E^{**}} = 1/2\ \nu_{E^{*}}$.

The steps described above occur at the disc's cytoplasmic surface, whereas the subsequent steps involve cytoplasmic cyclic GMP (cG) and its action on channels in the plasma membrane. In response to the ramping quantity of activated PDE, $E^{**}(t)$, the hydrolysis of cGMP accelerates, leading to a drop in $cG(t)$ with an onset that is initially parabolic. Analysis of the differential equations shows that the time-course of cyclic GMP decline can be described quite accurately as the right-hand half of a Gaussian expression (orange trace in Fig. 3*C*). At the very low concentrations of cyclic GMP that exist in the cytoplasm, the extent of CNGC ion channel opening by cyclic GMP is known to follow a power-law relation, with exponent $n \approx 3$. Accordingly, Lamb and Pugh (1992) deduced that the fraction $F(t)$ of open CNGC channels should likewise follow Gaussian kinetics, described by

$$F(t) = \exp\{-\frac{1}{2}\Phi A(t - t_{\text{eff}})^2\}, \quad \text{for } t > t_{\text{eff}}. \qquad (1)$$

Here, Φ is the flash intensity (in photoisomerizations per rod), A is the amplification constant (in units of s^{-2}), and t_{eff} is an effective delay time (of a few ms) that cumulates the contributions of several very short delay steps in the overall process (together with any delay caused by filtering of the electrical recording). The shape of this predicted time-course for the onset of the electrical response is shown as the red trace in Fig. 3*C*.

It has been shown that the outer segment ion channels behave almost as a current source; i.e. their current flow is almost independent of intracellular voltage over the physiological range. As a result, the circulating electrical current (as measured with a suction pipette) is simply proportional to $F(t)$.

The amplification constant, A, is specified as the product of three parameters

$$A = \nu_{E^{**}} \beta_{E^{**}} n \quad (2)$$

where $\nu_{E^{**}}$ is the rate (in s^{-1}) at which a single R* creates fully activated PDE**s (as shown by the continuous blue trace in Fig. 3); $\beta_{E^{**}}$ is the hydrolytic efficacy of an individual fully activated PDE** holomer, expressed as the rate constant at which a single PDE** decreases the cytoplasmic concentration of cyclic GMP; and $n \approx 3$ is the exponent in the power-law relation of channel opening by cyclic GMP.

Onset phase of the rod's response: comparison with experiment. Equation (1) has been shown to provide an excellent description of the onset phase of the rod's electrical response to brief flashes of light, over a wide range of intensities, across numerous species. As might be expected, the description is particularly good under conditions that reduce the effectiveness of the inactivation reactions; for example, in the case of infusion of the cytoplasm with the Ca^{2+} buffer BAPTA, in order to slow the elevation of guanylyl cyclase activity. One such experiment is illustrated in Fig. 4*A* for suction pipette recordings of fractional circulating current $F(t)$ from a salamander rod infused with BAPTA, in response to a series of brief flashes delivered at time zero; data from Torre et al. (1986). The red traces plot the predictions of eqn (1), using the measured flash intensities, together with a fixed value of amplification constant of $A = 0.08\ s^{-2}$ across all the traces, and clearly the fit of eqn (1) is very good.

Measurements of human rod photocurrents, obtained using the *a*-wave of the electroretinogram (ERG), are presented in Fig. 4*B*, again for brief flashes at a wide range of intensities, presented at time zero. As in the upper panel, the fit of eqn (1) shown by the red traces is very good at early times across all intensities. However, as indicated by the dotted extensions of the red traces, the experimental traces diverge from the predictions at later times, and this is almost certainly the result of the intrusion of signals originating elsewhere than in the rod outer segments; for example, from extracellular voltages elicited by ionic and capacitive currents in the inner segment (Robson & Frishman, 2014) as well as from the *b*-wave generated by bipolar cells.

For human rods, the amplification constant is typically found to be around $A \approx 4\ s^{-2}$, some 50-fold higher than for the amphibian rod in the upper panel, through a combination of differences of outer segment volume and of temperature, as will now be considered. Equation (2) characterizes the amplification constant, A, as the product of three parameters: $\nu_{E^{**}}$, $\beta_{E^{**}}$ and n. Of these, n is

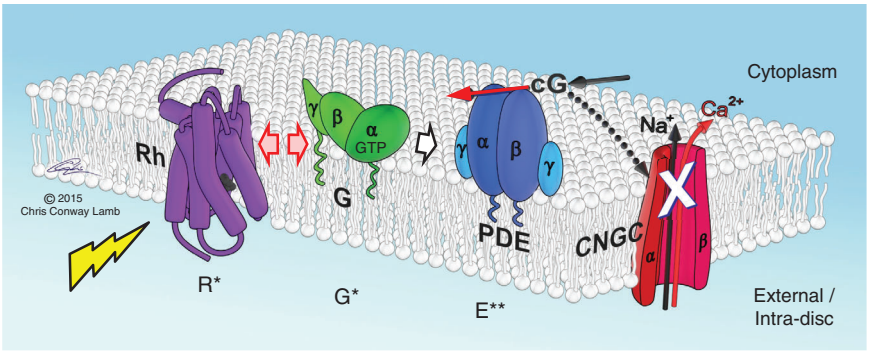

Figure 2. Activation steps in the phototransduction cascade
Schematic diagram of the proteins mediating the onset steps of phototransduction, and the flow of activation. The photopigment (rhodopsin, Rh, or its cone equivalent) traverses the lipid membrane. Upon absorption of a photon, its retinaldehyde chromophore is isomerized from the bent 11-*cis* configuration to the straight all-*trans* configuration, and within 1 ms this triggers conversion of the protein to an activated form, R* (metarhodopsin II), that is able to activate the G-protein cascade. Lateral diffusional motion (red arrow heads) causes repeated contacts between R* and the G-protein, transducin (G), leading to the activation of multiple transducins; as for other G-proteins, activation involves the release of GDP and binding of GTP to the α-subunit, whereupon the Gα·GTP is released as the activated form (G*). Further lateral diffusional contact (white arrow head) allows G* to bind to one of the two inhibitory γ-subunits of the phosphodiesterase (PDE). When each of its γ-subunits has bound a G* (i.e. with 2 G*s bound), the PDE becomes fully catalytically activated (E**); the singly bound form (E*, not shown) exhibits negligible activity. The fully activated E** hydrolyses (red arrow) cyclic GMP (cG), leading to a reduction in cytoplasmic cyclic GMP concentration, and hence to closure (X) of cyclic nucleotide-gated channels (CNGCs) in the membrane. Note that, as drawn, the membrane topology applies to cone photoreceptors, where all of the transduction proteins reside in the plasma membrane; for rods, most of the transduction proteins are restricted to the disc membranes, with only the CNGCs (of the illustrated proteins) residing in the plasma membrane. On the other hand, as drawn, the PDE represents the rod version comprising α plus β catalytic isoforms, whereas the cone version comprises a pair of α' catalytic isoforms. Modified from Lamb et al. (2016).

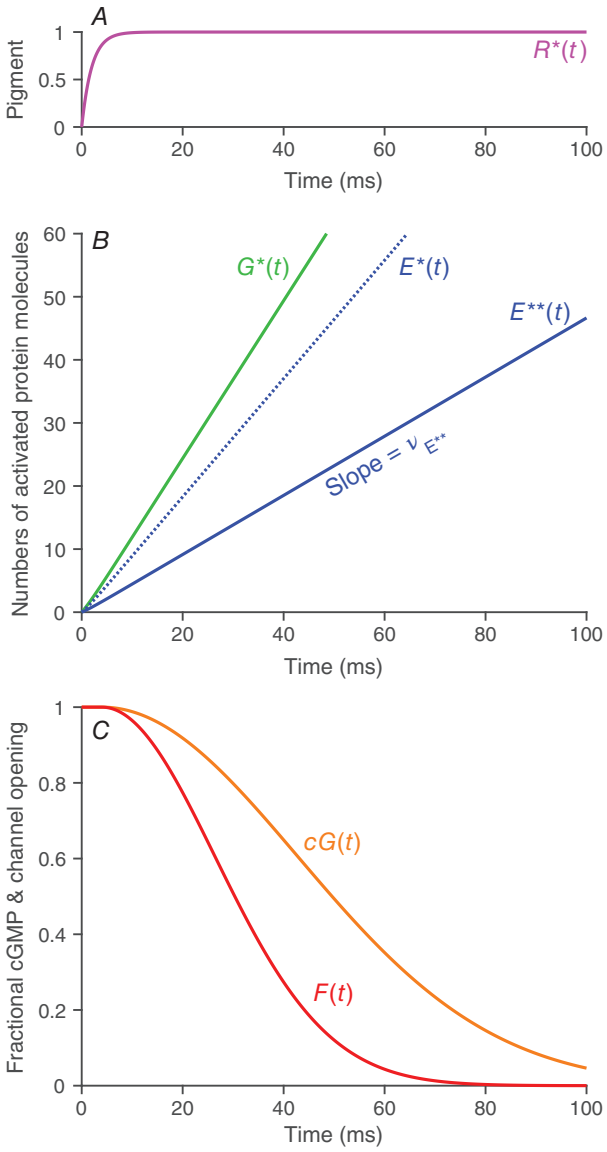

Figure 3. Predicted kinetics and amplification of the rod phototransduction cascade
Simplified model for kinetics of phototransduction activation when shut-off reactions are ignored; the time scale is applicable to mammalian rods. *A*, in response to a single photoisomerization at time zero, a single R* is activated after a short delay, and (in the absence of inactivation) it remains present (purple trace). *B*, that R* activates transducins G* at a constant rate, so that $G^*(t)$ ramps with time (green trace), with a slope $\nu_{G^*} \approx 1250$ G*/s. Individual subunits of E* are activated at a somewhat lower rate (ν_{E^*}, dashed blue trace), and the rate of activation of doubly bound E** holomers is half that; i.e. $\nu_{E^{**}} = 1/2\ \nu_{E^*}$ (blue trace). *C*, kinetics of fractional cyclic GMP concentration, $cG(t)$ (orange trace), and fractional channel opening, $F(t)$ (red trace), for a flash that delivered Φ photoisomerizations. The ramp-wise activation of PDE hydrolytic activity causes $cG(t)$ to decline, with a shape that is initially parabolic, and the cube-law relation between cyclic GMP concentration and channel activity thereby causes $F(t)$ to fall as the cube of $cG(t)$. When inactivation reactions can be ignored, mathematical analysis shows that the predicted time-course of fractional channel opening is given by eqn (1).

expected to be unaltered by volume or temperature, but $\nu_{E^{**}}$ is likely to be strongly temperature-dependent, while $\beta_{E^{**}}$ will be inversely proportional to the cytoplasmic volume of the outer segment (because $\beta_{E^{**}}$ is defined in terms of the rate of change of the mean concentration of cyclic GMP throughout the outer segment). As the rod outer segment volume in mouse is ~1/20 that in salamander, the activity of the PDE**s is concentrated into a 20-fold smaller cytoplasmic space, and hence $\beta_{E^{**}}$ is higher; this volume factor accounts for ~20× of the 50-fold ratio. The temperature difference from room to

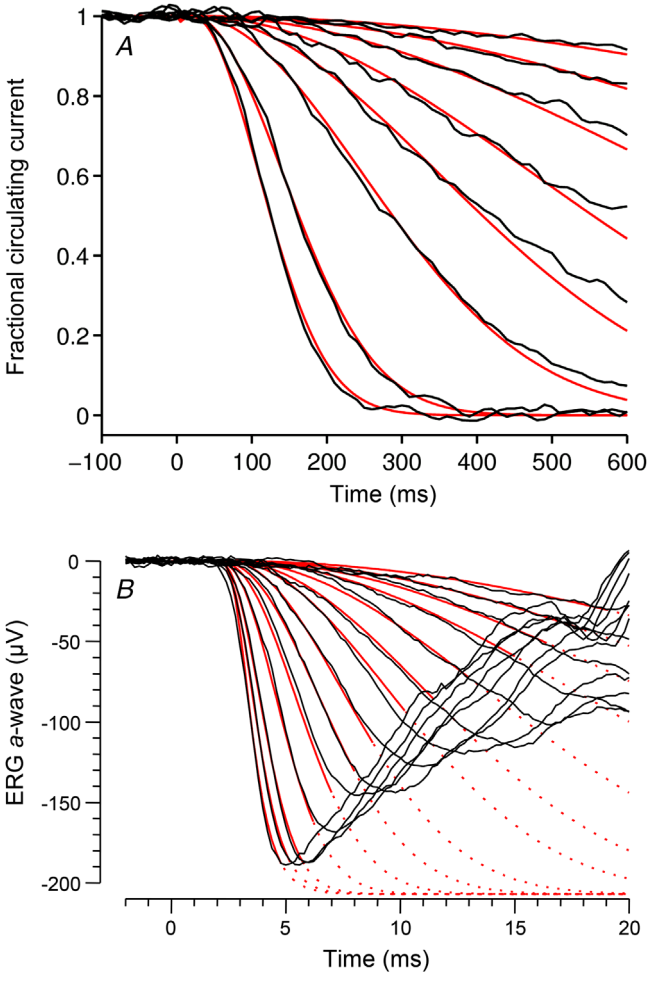

Figure 4. Measured and predicted rising phase kinetics
In both panels, the black traces are experiments, for brief flashes delivered at time zero, and the red traces are the predictions of eqn (1), using the measured light intensities. *A*, amphibian rod suction pipette recording, after the Ca^{2+} buffer BAPTA had been trapped in the rod's cytoplasm, for flashes delivering from $\Phi \approx 10$ to 2000 photoisomerizations; fitted amplification constant $A = 0.08\ s^{-2}$. Modified from Pugh and Lamb (1993); data from Torre et al. (1986). *B*, human ERG *a*-wave recordings, for flashes estimated to have delivered from $\Phi \approx 300$ to 500 000 photoisomerizations; fitted amplification constant $A = 3.9\ s^{-2}$. Modified from Friedburg et al. (2001).

body temperature accounts for the remaining 2−3×, probably in the main part because the resultant increase in disc membrane fluidity increases the rate of molecular contact, and thereby increases $\nu_{E^{**}}$; see Calvert et al. (2001) for experiments on the role of disc membrane fluidity on amplification constant.

Application of eqn (2) to experimental recordings thereby provides a means of extracting the product $\nu_{E^{**}}\ \beta_{E^{**}}$, but there can be considerable difficulty in assigning individual values to those two parameters. Later, in *Extraction of the rate of transducin activation*, an independent approach will be presented for estimating the rate $\nu_{E^{**}}$ of activation of PDE per isomerization from properties of the response recovery following intense flashes.

Response recovery in rods: shut-off, Ca^{2+} feedback and role of dimeric PDE6. In order to terminate the activity of the transduction cascade, it is necessary to terminate rhodopsin's activity, to terminate transducin/PDE activity, and to raise the concentration of cyclic GMP back to its resting level.

Termination of rhodopsin's activity. Termination of R* activity involves (i) phosphorylation by rhodopsin kinase (encoded by *GRK1*) of Ser and Thr residues in rhodopsin's C-terminus, which enables (ii) the binding of arrestin, thereby 'capping' rhodopsin's catalytic site and hence preventing further activation of transducin.

Termination of transducin/PDE activity. Termination of G* activity results from hydrolysis of the terminal phosphate of the GTP that had bound to Gα during its activation. Such GTPase activity is intrinsic to the Gα protein, but its rate is accelerated when the Gα binds to the PDE6 γ-subunit during activation of the PDE, and then greatly accelerated upon binding of the RGS9 (regulator of G-protein signalling 9) to form a Gα·PDEγ·RGS9 complex (see also next section). The assumption is usually made that at the instant that the terminal phosphate is hydrolysed, Gα unbinds from the PDEγ, so that the PDE's hydrolytic activity instantly ceases.

Calcium feedback regulation. When the CNGC channels in the cell's plasma membrane close in response to lowered cytoplasmic cGMP concentration, the influx of cations (primarily Na^+, but also Ca^{2+}) is reduced. This not only generates the rod's electrical response, but it also causes a pronounced reduction in the cytoplasmic Ca^{2+} concentration, because initially the extrusion of Ca^{2+} by the $Na^+/Ca^{2+}/K^+$-exchanger (NCKX) continues (see Fig. 7 below). The lowered Ca^{2+} concentration has a potent effect in activating two guanylyl cyclase-activating proteins (GCAP1 and GCAP2, encoded by *GUCA1A* and *GUCA1B*), causing the two guanylyl cyclase enzymes (GC-E and GC-F, encoded by *GUCY2D* and *GUCY2F*) to synthesize cyclic GMP at an elevated rate. Overall, this system provides a very powerful negative feedback loop, whereby a reduction in cyclic GMP concentration triggers vigorous synthesis of cyclic GMP. The net effect is to create a very strong stabilizing mechanism that provides the cell's most important means of light adaptation, because a very large increase in steady PDE activity is accompanied by only a relatively small reduction in the steady level of cyclic GMP. In addition, cytoplasmic Ca^{2+} concentration has relatively minor effects on other proteins (including recoverin) but these effects do not appear to be of great importance to the light response.

R shut-off kinetics.* Many studies modelling the recovery phase of the rod's response to light have made the assumption that the R* activity declines exponentially with time, but this will be at best a rough approximation. For single-photon responses, some studies have adopted a model in which R*'s activity declines sequentially with each added phosphate, as reported by Gibson et al. (2000); see Hamer et al. (2003), Reingruber and Holcman (2008), Caruso et al. (2010), Gross et al. (2012), Reingruber et al. (2013). However, subsequent analysis of single-photon response kinetics has not supported that suggestion, and has instead supported the view that the dominant event in the shut-off of an individual R* is the binding of arrestin, which leads to an abrupt decline in activity (Lamb & Kraft, 2016).

Differences in cone phototransduction parameters. The responses of cone photoreceptors are much briefer than those of rods (at a given temperature), as a result of much faster shut-off steps. From a range of different experimental approaches, estimates of the four time constants that contribute to response recovery in human cones indicate that all four are very fast, in the range of 3−18 ms (Lamb, 2010). Although there is uncertainty in determining which time constant corresponds to which step, the following allocation of mean lifetimes has been suggested: lifetime of activated cone photopigment, $\tau_R \approx 3$−5 ms; lifetime of activated transducin/PDE, $\tau_{PDE} \approx 9$−18 ms; turnover time for cytoplasmic Ca^{2+} concentration, $\tau_{Ca} \approx 3$ ms; and (under strongly light-adapted conditions) the turnover time for cytoplasmic cyclic GMP becomes as short as $\tau_{cG} \approx 4$−6 ms (see Table 1 of Lamb, 2010).

The details of the mechanistic differences that permit cone photoreceptors to attain such rapid recovery are not fully understood. For the rapid shut-off of the cone opsin, it would seem that the cone kinase (GRK7) and cone arrestin (Arr3) must act extremely rapidly. The more rapid shut-off of cone transducin/PDE is almost certainly the result of the higher concentration of RGS9 (regulator of G-protein signalling 9), which accelerates the GTPase activity; the three proteins making up the

RGS9 complex are identical in rods and cones, but their expression level is an order of magnitude higher in cones than in rods (Cowan et al., 1998; Zhang et al., 2003). The shorter turnover time for cytoplasmic Ca^{2+} presumably results from the far higher surface-to-volume ratio of plasma membrane, due to the fact that the cone sacs are evaginations (rather than being sealed off as discs in rods). Finally, the shorter turnover time for cyclic GMP is likely to result from a higher steady activity of PDE in the presence of bright light. Thus, as is the case in rods (Nikonov et al., 2000), this latter time constant in cones will shorten during light adaptation, and thereby speed the response kinetics. With three of its four time constants each around 3−5 ms and with the remaining one around 10−20 ms, the cone is able to respond appreciably to square-wave illumination that has a period of 10 ms or even less, and as a result a strongly light-adapted human observer can detect flickering light at frequencies above 100 Hz.

The gain of phototransduction appears to be lower in cones than in rods, though this factor is less pronounced than the difference in kinetics. However, it is difficult to measure the gain parameters accurately for several reasons: firstly because of the extremely short lifetimes involved, secondly because of potential issues with light intensity calculations *in vivo*, and thirdly because of the difficulty in obtaining purified proteins for *in vitro* study; as a result there is some uncertainty about the precise values of the various gain parameters for cone phototransduction. The parameters of the biochemical reactions involved in cones *vs*. rods have been thoroughly studied in fish photoreceptors by Kawamura and Tachibanaki (2008).

Prediction of the rod's bright-flash response recovery kinetics. A major factor that has been overlooked in the majority of studies that have modelled photoresponses relates to the dimeric nature of the PDE. In most models, the effects of the two transducins binding to the two PDEγ subunits have been assumed to be independent of each other, and additive. However, evidence has been accumulating over decades for a non-linearity in the effect of the first and second binding events, and recent evidence has shown this non-linearity to be very pronounced (Qureshi et al., 2018); thus, the binding of a single transducin elicits at most ∼5% of the full hydrolytic activity that is elicited by the binding of two transducins to the PDE holomer. This phenomenon is predicted to provide considerable immunity from thermal noise within the phototransduction cascade (i.e. from thermal activation of transducin activity); it thereby plays an important role in aiding the detectability of single-photon events, and as such is crucial to visual performance in the scotopic system under starlight conditions. Additionally, though, allowance for this phenomenon is critical for correct calculation of the rate of transducin activation elicited by a single R^*, as will be addressed below.

The time-course of bright-flash recovery predicted when allowance is made for dimeric activation of the PDE is presented in Fig. 5, using simulations from Lamb and Kraft (2020). Figure 5*A* shows the predicted kinetics of fully activated PDE dimers, E^{**}, where the saturation level corresponds to the entire complement of a little over 100 PDE holomers activated per disc surface (with around 1400 disc surfaces per mammalian rod outer segment). The blue traces (which are mostly hidden by red traces) are for a straightforward model of dimeric PDE activation and recovery, while the red traces additionally take account of a tiny proportion of rhodopsin molecules that have been reported to exhibit 'aberrant' shut-off. Thus, around 0.2% of the rhodopsin molecules fail to shut-off normally (possibly as a result of proteolysis of the rhodopsin molecule's C-terminal region, containing the Ser and Thr residues that need to be phosphorylated before arrestin can bind), causing a slow tail in recovery for intense flashes; this tail appears quite minor for the recovery of E^{**} in Fig. 5*A*.

However, when the electrical response is calculated (see Fig. 5*B*), the predicted late tail with intense flashes is much more pronounced; this occurs because (as indicated by the dashed line in Fig. 5*A*) only a very small fraction of the PDE needs to be activated in order to saturate the electrical response (indicated by the corresponding dashed line in Fig. 5*B*). Comparison of these predicted responses with the published experiment of Burns and Pugh (2010) for a wild-type (WT) mouse rod, in Fig. 5*C*, shows a good description of the main qualitative features of the recorded rod photoresponses.

By measuring the time T_{sat} taken to recover from saturation (i.e. until the current crosses the dashed line drawn at 10% recovery in Fig. 5*B*), one can plot T_{sat} as a function of flash intensity, both for the predictions of the model and for the experimental results, as is done in Fig. 6. When plotted against flash intensity on a logarithmic scale, this relationship is characterized to two approximately straight-line regions. The slopes of the relationship in these regions represent what have been referred to as two 'dominant time constants' of recovery, of roughly $\tau_{D1} = 245$ ms and $\tau_{D2} = 780$ ms, respectively. For WT mouse rods, the intersection of the two straight lines occurs at an intensity, termed the 'transition intensity', of $\Phi_{trans} \approx 5000$ photoisomerizations/rod, the significance of which will now be examined.

Extraction of the rate of transducin activation. The magnitude of the transition intensity provides an important means of estimating the rate at which molecules of transducin are activated by a single photoisomerization (Lamb & Kraft, 2020). As proposed by

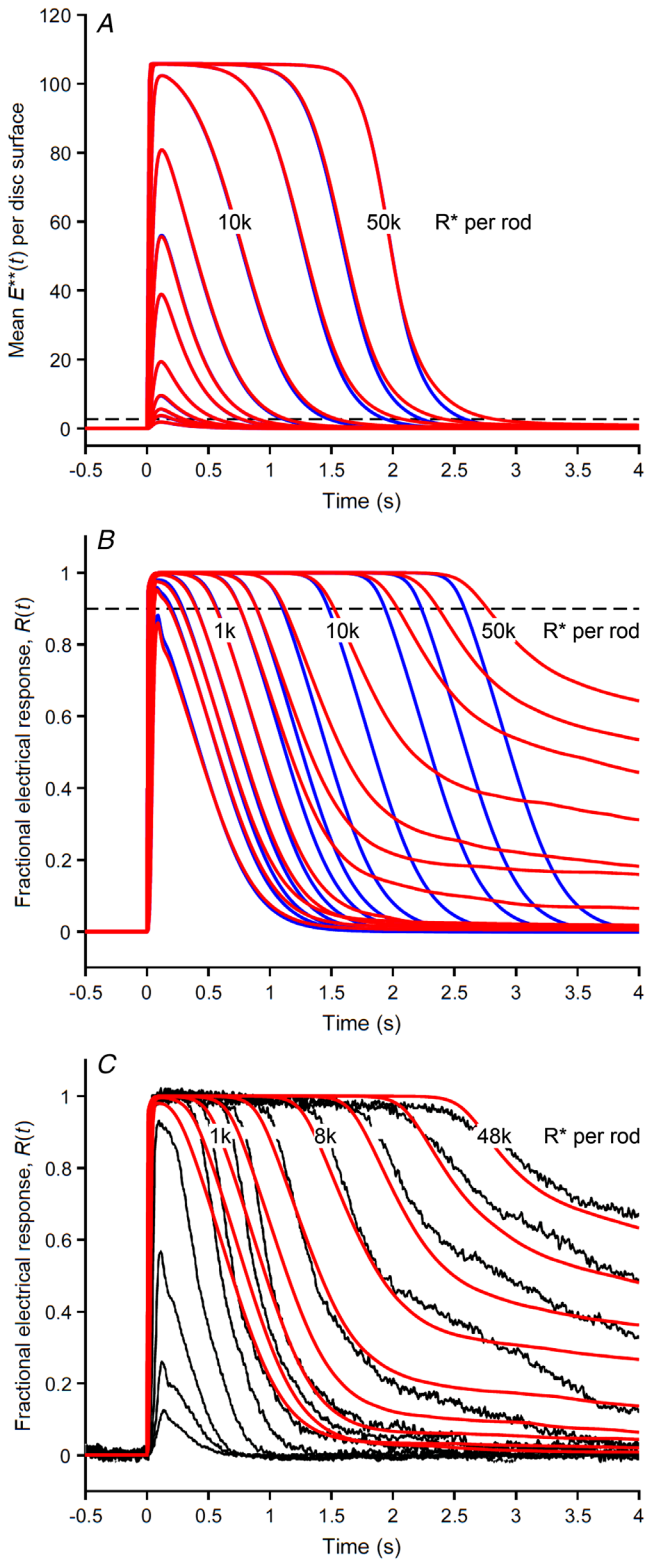

Figure 5. Bright-flash recovery kinetics
Predictions of bright-flash response kinetics for a model that takes account of the dimeric nature of the PDE. Blue traces are for the basic model; red traces additionally allow for a very low probability (0.2%) of occurrence of aberrant shut-off of activated rhodopsins, R*. *A*, predicted kinetics of PDE activity, $E^{**}(t)$, for flashes delivering Φ = 100, 200, 300, 500, 1000, 2000, 3000, 5000, 10,000, 20,000, 30,000 and 50,000 R*. The saturating level corresponds to activation of the full complement of 106 PDE holomers per disc surface. *B*, predicted kinetics of fractional electrical response, $R(t) = 1 - F(t)$, for the same flash intensities. Note the substantial slow tail component for the red traces, which result from aberrant R* shut-off events. The dashed horizontal line in *B* indicates recovery from saturation, defined as a criterion level of 10% circulating current; for comparison, the dashed line in *A* indicates the corresponding level of $E^{**} \approx 2.5$ activated holomers that is needed to saturate the electrical response. *C*, black traces are suction pipette recordings from a wild-type mouse rod, to flashes delivering from $\Phi \approx 4$ to 48 000 R*; data from Burns and Pugh (2010). Red traces are predictions for the brightest nine of those intensities, that caused response saturation. Predicted traces are from Lamb and Kraft (2020).

Martemyanov et al. (2008), the transition intensity occurs when every PDE6 dimer in the outer segment has just been covered by transducins. Given that the expression level of PDE6 dimers is 1/300 to rhodopsin (Pentia et al., 2006), a mammalian rod outer segment contains ~140,000 PDE6 dimers/rod, so that an intensity of

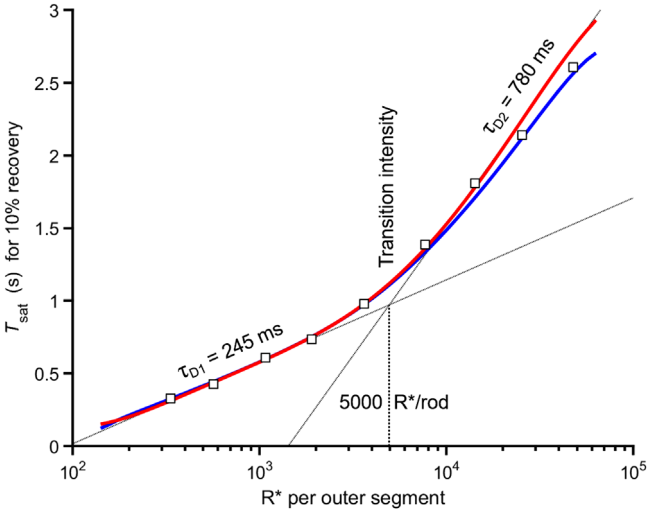

Figure 6. Time spent in saturation, dominant time constant, and transition intensity
The time that the response spends in saturation, T_{sat}, defined as the time to recover to 10% circulating current, is plotted against flash intensity, Φ, in semi-logarithmic coordinates, for both theory and experiment from Fig. 5. The symbols plot the time spent in saturation for the wild-type mouse rod recorded by Burns and Pugh (2010); the blue and red curves plot the model predictions either without (blue) or with (red) allowance for aberrant R* shut-off. For the lower saturating intensities (up to $\Phi \approx 2000$ isomerizations) both experiment and theory are well described by a straight line, corresponding to a so-called dominant time constant of $\tau_{D1} = 245$ ms; for the brightest intensities the data are again approximately described by a straight line, though with a steeper slope corresponding to $\tau_{D2} \approx 780$ ms. The transition between these two regimes occurs at a transition intensity of $\Phi_{trans} \approx 5000$ isomerizations. This value is used in the text to estimate the rates of activation of transducin and the PDE. Modified from Lamb and Kraft (2020).

$\Phi_{trans} \approx 5000$ photoisomerizations/rod corresponds to 140,000/5000 = 28 E**/photoisomerization, and hence to at least 56 G*/photoisomerization. However, not every G* that is activated has the opportunity to bind to the PDE6, because inactivation is occurring simultaneously, and the modelling suggests that, to cover the required 56 PDE6γ subunits, the number of G*s activated must be around 85 G*/photoisomerization. Finally, as the mean lifetime of each R* is only $\tau_R \approx 68$ ms (Lamb & Kraft, 2016), the rate of transducin activation needs to be 85 G*/68 ms, or $\nu_{G^*} \approx 1250$ G* s^{-1} per R*.

This rate of transducin activation, of >1000/s, calculated from analysis of bright-flash responses, conforms to estimates obtained from light-scattering measurements (Heck & Hofmann, 1993; Vuong et al., 1984). On the other hand, it is around 4–8-fold higher than has previously been assumed in modelling studies (Gross et al., 2012), or observed to date using biochemical approaches (Leskov et al., 2000). However, in the modelling studies there are other parameter values that could trade off against the assumed rate of activation, and biochemical measurements *in vitro* cannot necessarily replicate *in vivo* conditions. Accordingly, it seems appropriate to adopt the higher values obtained from bright-flash and light-scattering studies.

Recently, Yue et al. (2019) adopted two approaches, aimed at measuring the amplitude of individual transducin/PDE activation events in mouse rods; firstly, they used a mutant rhodopsin that had an extremely low probability of activating transducin, and secondly they examined bleach-induced noise at late times after light exposure. Their analysis suggested that the single-photon response represented the summation of only 12–14 G*-PDE* events, or around one-sixth of the number of G*s estimated above. Some potential problems with that analysis were described by Heck et al. (2019), including that the underlying transducin/PDE events they observed were likely to have corresponded to E** activations and hence to two G*s, so that their number would have increased to 24–48 G*s per R*. Future work will be required to resolve the remaining differences.

Evolutionary origin of cone/rod isoforms of transduction proteins

In most cases, the proteins mediating phototransduction are present as different isoforms in rod and cone photoreceptors; these different isoforms are not simply splice variants, but are instead encoded by different (but paralogous) genes in rods and cones. Figure 7

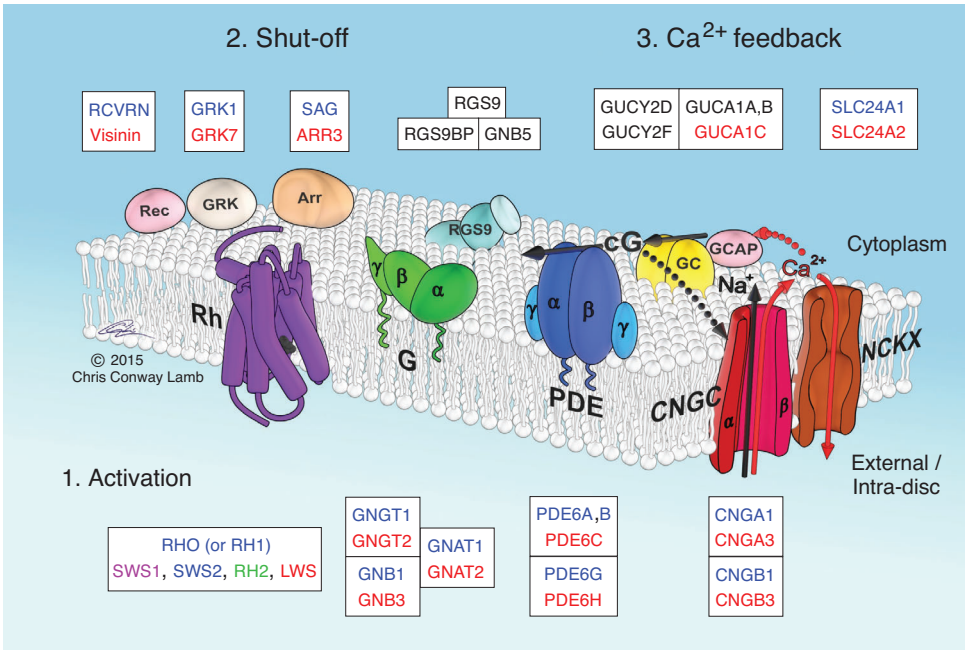

Figure 7. Genes encoding the proteins of phototransduction
Schematic representation of the proteins involved not only in response activation, but also in response shut-off and Ca^{2+}-feedback regulation, together with identification of the HGNC names of the genes encoding the cone-specific (red), rod-specific (blue) and common (black) isoforms. Proteins not previously identified in Fig. 1 are as follows. Rec: recoverin or visinin. GRK: G-protein receptor kinase. Arr: arrestin. RGS9: regulator of G-protein signalling 9. GC: guanylyl cyclase. GCAP: guanylyl cyclase activating protein. NCKX: sodium/calcium-potassium exchanger. Modified from Lamb (2020).

identifies the HGNC names of the phototransduction genes (as defined by the HUGO Genome Nomenclature Committee), with blue and red denoting isoforms that are expressed exclusively in rods or in cones, respectively. Eleven of these protein subunits (making up seven protein holomers) are present as distinct rod/cone isoforms, and are shown in colour. The remaining seven protein subunits shown in black are encoded by common genes in the two classes of photoreceptor: these comprise the three subunits of the RGS9 complex, and the two guanylyl cyclases and their guanylyl cyclase activating proteins (GCAPs) (Fig. 7).

How did this come about? In other words, what was the origin of distinct genes in two classes of sensory receptor that have fundamentally the same function: the detection of light? The answer to these questions reinforces the view of Dobzhansky (1973) that 'Nothing in biology makes sense except in the light of evolution'. As will now be examined, this rod *vs*. cone distinction of isoforms arose in a single event: the first round (1R) of the two rounds of whole-genome duplication (2R-WGD) that occurred roughly 600 Mya (million years ago) in a proto-vertebrate ancestor of ours. To investigate this, we first need to consider the evolution of vertebrates.

Origin of vertebrates: two rounds of genome duplication. From the perspective of the evolution of jawed vertebrates (gnathostomes), a summary of the important speciation events that occurred over the course of the last 800 My is sketched in Fig. 8*A*, where the timings are a composite from several recent studies (Dohrmann & Wörheide, 2017; dos Reis et al., 2015; Kumar et al., 2017); this diagram concentrates on extant lineages, and ignores extinct lineages. Around 700 Mya, the descendants of a simple bilaterally symmetric organism diverged to form protostomes (that include the great majority of what we usually think of as 'invertebrates') together with our own lineage of deuterostomes (named on the basis that, developmentally, the second opening becomes the mouth). Within deuterostomes, chordate organisms (characterized by a notochord) have existed for over 600 My, with our own ancestors having diverged successively from lineages that gave rise to lancelets (such as *Amphioxus*) and tunicates (such as the sea squirt, *Ciona*).

Sometime, roughly between 600 and 500 Mya, our proto-vertebrate ancestor underwent two successive rounds of whole-genome duplication (2R-WGD), marked in Fig. 8*A* by '1R' and '2R', respectively, that led to a doubling and then another doubling of the organism's chromosomes, and hence of all its genes. After each of those genome duplications, extensive loss of genes occurred, with the result that for many of the ancestral genes only a single copy was retained. But in numerous other instances, either two or three, or even all four of the replicated genes survived. Today, the human genome comprises over 200 gene families that retain all four paralogs that arose during 2R-WGD, so that more than 800 of the roughly 20,000 human protein-coding genes represent such quadruplicate paralogs.

The first of these genome duplications (1R) occurred in a proto-vertebrate organism, prior to the divergence of what would become the jawless and jawed vertebrate lineages. The second such duplication (2R) occurred at the base of the jawed vertebrate (gnathostome) lineage; note that jawed vertebrates are denoted by the red lines in Fig. 8*A*. Many other instances of genome duplication have occurred in various lineages: notably at the base of the teleost fishes, as well as within the jawless vertebrates, and in various protostome taxa, etc. However, the only genome duplication events relevant to placental mammals are the two indicated as 1R and 2R.

The mechanisms that gave rise to the two genome duplications appear to have been different. 1R is thought to have been an 'autotetraploidy' event, whereby an error in DNA replication generated two copies of the entire genome; 2R is thought to have resulted from 'allotetraploidy', whereby two related diploid organisms hybridized, thereby combining two somewhat different genomes. Whatever the mechanisms, the crucial point is that, by the time that the first jawed vertebrates appeared (somewhere around 500 Mya), a quadruplication of the ancestral chordate genome had occurred, followed by the loss of many individual genes.

Evidence for genome quadruplication by 2R-WGD: paralogons. What is the evidence that such quadruplication of the entire set of genes occurred at the base of the jawed vertebrate lineage? The most obvious telltale sign is the occurrence of up to four closely similar copies (paralogs) of each of numerous genes within every jawed vertebrate species, in conjunction with the arrangement of those genes in similar patterns across paralogous regions on sets of four chromosomes. Such paralogous regions are termed 'paralogons', and the concept of their origin is illustrated in Fig. 8*B*.

The lower part of Fig. 8*B* shows the arrangement of selected genes (including those for the visual opsins and transducin) on four chromosomes of the spotted gar genome. This species is a convenient ray-finned fish, for which the genome has been assembled at a chromosome level, and which, as a non-teleost, did not undergo the teleost-specific 3R duplication. Inspection shows that these four chromosomes (LG5, LG1, LG8 and LG3) possess multiple sets of four paralogous genes – for example, the genes for the mGluRs and for the Cav1s. The numbering beneath the gene names gives the position (in mega base-pairs, Mbp) of each gene on its chromosome;

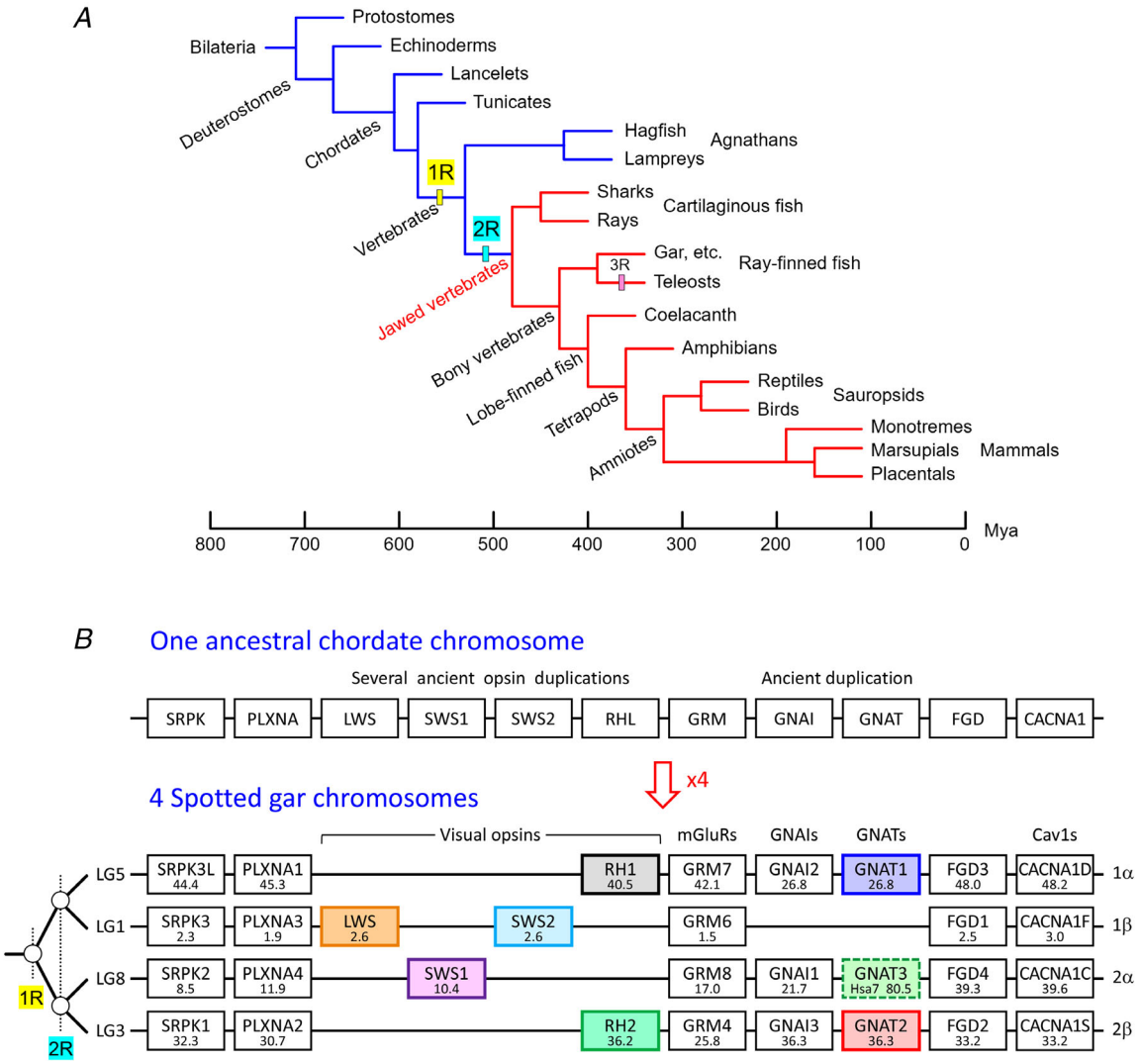

Figure 8. Vertebrate evolution and 2R-WGD quadruplication of genes
A, evolutionary tree of branching pattern for extant lineages of interest, with emphasis on jawed vertebrates (gnathostomes) shown by red lines. Note that each of the illustrated taxa persists to the present, and that the endings of the horizontal lines do not indicate extinctions. The approximate timings of speciation events that generated the different lineages are indicated, with a time-scale of millions of years ago (Mya), but it is important to realize that there is considerable uncertainty about the precise timings, with the level of uncertainty increasing for the more ancient splits; the timings shown here represent a composite based on several studies (Dohrmann & Wörheide, 2017; dos Reis et al., 2015; Kumar et al., 2017). The two rounds of whole genome duplication that preceded the ancestral gnathostome are indicated '1R' and '2R'. Teleost fish experienced a third genome duplication, indicated '3R'; they, and other individual species (such as *Xenopus laevis*) that have experienced additional genome duplication(s), are generally more complicated to analyse, and have been excluded from the analysis presented. *B*, schematic representation of the quadruplication of genes during 2R-WGD. The top row depicts a hypothesized set of genes along a single chromosome of our chordate ancestor prior to either round of genome duplication. The lower four rows depict four chromosomes (LG5, LG1, LG8 and LG3) in spotted gar, a ray-finned fish that diverged before teleosts arose, and that has not undergone any genome duplication subsequent to 2R. The four chromosomes contain numerous sets of paralogous genes, that have up to four members present. Each box represents an individual gene, and the number beneath the gene name gives the position of that gene (in mega-base pairs, Mbp) from the start of the chromosome. The genes have been repositioned along each chromosome so as to emphasize the existence of paralogous families. For the *GNAT* family (transducins) the colouring indicates: blue, rod-specific; red, cone-specific; green, expressed elsewhere than rods or cones, and this convention is continued in Fig. 9. (In mammals, *GNAT3* encodes gustducin and is expressed in some taste receptor cells; the gene has been lost in ray-finned fish, and the dashed box gives its position in the human genome.) Colouring of the visual opsin genes provides an approximate representation of the spectral sensitivity of the expressed opsins.

in the case of chromosome LG1, all seven of the illustrated genes are localized within 1.5 Mbp of each other, though such close proximity is rather atypical.

The upper part of Fig. 8*B* sketches the hypothesized arrangement of a single copy of each gene on a region of one chromosome in the ancestral chordate organism, prior to 1R. Following the two rounds of genome duplication, some of the ancestral genes are now represented by four paralogs located on the four illustrated chromosomal regions; however, in many cases there has been loss of one or more of the daughter genes. For example, for the visual opsins, which had undergone several ancient local duplications earlier in deuterostome evolution, only a single copy of each was retained for the *LWS*, *SWS1* and *SWS2* genes utilized by cones; interestingly, two copies of an 'RH-like' (*RHL*) gene were retained, with one of these (*RH2*) remaining as a cone opsin, and the other (*RH1*) becoming the ancestral rhodopsin.

For the transducins, it is now clear that the *GNAI* gene for an inhibitory G-protein underwent a local tandem duplication within chordates, which led to the presence of *GNAI* and *GNAT* genes immediately adjacent to each other. Then, following the 2R-WGD quadruplication, one *GNAI–GNAT* pair was lost, but the remaining three *GNAI–GNAT* pairs have been retained, and in the majority of extant jawed vertebrate species each such pair remains in close proximity. (*GNAT3* in Fig. 8*B* is shown in dashed outline because the *GNAT3* gene has been lost in all ray-finned fish; because of that loss, this panel shows the human gene, which is located in a syntenic position.)

Paralogon arrangement of phototransduction genes. The paralogon arrangement of another 15 phototransduction genes (from six families of paralogs) is illustrated in Fig. 9*A*. Four paralogons are shown, three of which (paralogons 14, 15 and 17) each contain one family of phototransduction paralogs (*PDE6*s, *CNGA*s and *GNB*s), while the other (paralogon 16) contains three such families (arrestins, guanylyl cyclases and *GRK*s). The coloured shading denotes the following: red shading is for isoforms specific to cones, blue is for isoforms specific to rods, grey is for isoforms common to both rods and cones, and green is for isoforms expressed elsewhere than in rods or cones.

Analysis of the vertebrate karyotype detected the existence of 17 paralogons in jawed vertebrates (Lamb, 2021; Sacerdot et al., 2018; Simakov et al., 2020). However, the most recent study (Nakatani et al., 2021) has revised this number to 18 paralogons, because one of those described previously (termed paralogon 14 by Lamb, 2021; Sacerdot et al., 2018) should properly be sub-divided into two.

One feature that is not illustrated in either Fig. 8*B* or 9*A* is that, during the >500 My since 2R-WGD, there has been extensive 'shuffling' of genes within each chromosome, as a result of inversions, and in addition there have been numerous instances of chromosome fusions and fissions in different lineages. Those multiple historical events complicate the analysis of chromosomal positions, yet they have not obscured the signature of 2R-WGD within the genome.

Pattern of branchings: molecular phylogeny. Although Fig. 8*B* indicates those pairs of chromosomes that diverged from each other at 1R, conclusive evidence for this identification is not contained in that figure, and instead must be obtained by other analysis. One such line of evidence is contained in the molecular phylogenies of Fig. 9*B*, and for certain paralogons, an independent line of evidence can be found in Fig. 9*A*.

Figure 9*B* presents summary molecular phylogenies for one four-membered family from each of the five paralogons shown in Figs 8*B* and 9*A*. In these 'collapsed' phylogenies, every triangle plots a clade of mRNA sequences for the jawed vertebrate gene named to its right; the vertical extent of each triangle is proportional to the number of sequences analysed (typically ∼25 per clade) and the horizontal width provides a measure of the degree of evolutionary divergence of those molecular sequences within the clade. Importantly, the numbers immediately to the left of each triangle give the percentage 'bootstrap support' for the likelihood that those sequences do indeed form a clade, while the numbers at each branch give the percentage support for the indicated branching pattern. Thus, for paralogon 5 (Fig. 9*B*, left) there is unanimous support for each of the four clades, as well as unanimous support for each of the three branchings. Note that, to save space, the 'outgroup' sequences that were used to locate the root of the tree in each panel have not been shown; the entire phylogenies, in fully expanded form, have been presented in the Supplementary Material of Lamb (2021).

Incredibly, for each of the five collapsed trees in Fig. 9*B*, there is unanimous (i.e. 100%) support for every node, with just a single exception: for paralogon 17, one of the nodes has 96% support. In each case, this provides overwhelming confirmation for the illustrated pattern of branching at 1R; that is, showing that the upper pair of clades diverged from the lower pair of clades at the first round of whole-genome duplication. (Note that the arrangement of clades from top to bottom has been preserved, for corresponding paralogons in Figs 8 and 9.)

A second line of verification is evident, for the four paralogons illustrated in Fig. 9*A*, from the contiguity of subsets of chromosomal regions between those paralogons. Thus, the lower pair of chromosomes are common across paralogons 14 and 15, and then

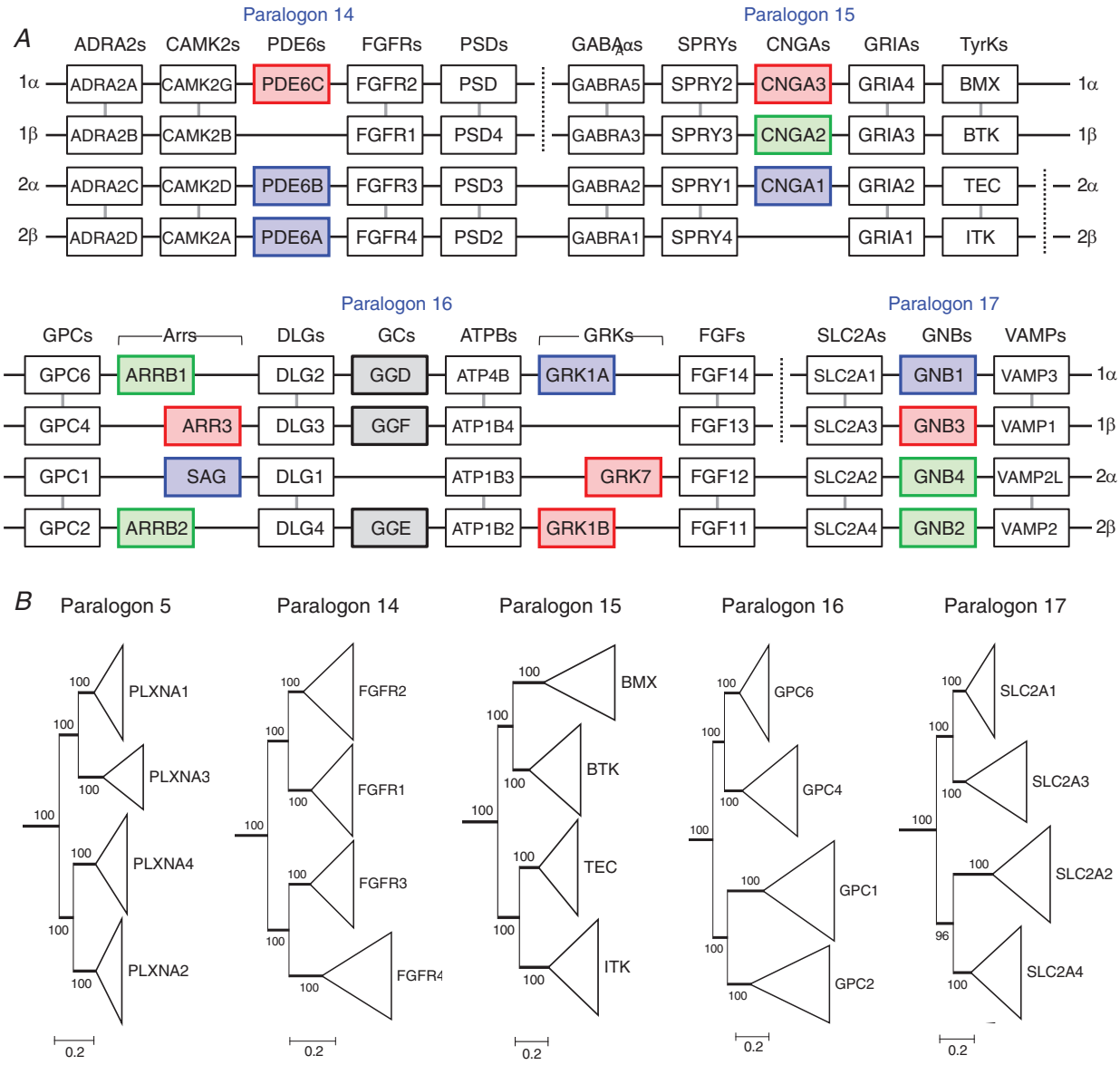

Figure 9. 2R-WGD: paralogons and molecular phylogeny
A, example gene families on four paralogons that contain phototransduction genes. These paralogons have been identified through comparisons of chromosomes across a broad range of jawed vertebrate species; the paralogon numbering is that adopted by Sacerdot et al. (2018) and Lamb (2021), and the row numbering is that adopted by Simakov et al. (2020); see also Nakatani et al. (2021). Paralogon 14 includes the *PDE6*s; paralogon 15 includes the *CNGA*s; paralogon 16 includes the arrestins, the GCs and the *GRK*s; and paralogon 17 includes the *GNB*s (that encode the transducin β-subunits. For each of these paralogons, three or four other example families of genes are illustrated, chosen from amongst those families that retain all four quadruplicates (all four paralogs). As discussed in the text, it is clear that in each of the illustrated paralogons the upper pair of chromosomes (labelled 1α, 1β) diverged from the lower pair (labelled 2α, 2β) at the first round of genome duplication, 1R. Colouring of genes: blue, rod-specific; red, cone-specific; grey, expressed in both rods and cones; green, expressed elsewhere than rods or cones. *B*, maximum likelihood molecular phylogenies for an example family of genes from each of the five paralogons shown either in *A* or in Fig. 8*B*. The fully expanded version of each of these collapsed phylogenies has been presented in the supplementary material of Lamb (2021), along with the outgroup (which is not shown here). In each panel, the clades (triangles) are arranged from top to bottom in the same order as in *A* and in Fig. 8*B*. Each triangle represents around 25 protein sequences from jawed vertebrates, with the vertical height of the triangle proportional to the actual number of sequences used; the horizontal width of each triangle provides a measure of sequence variation across those sequences, with the scale bar in amino acid substitutions per residue. The numbers at each node denote the percentage bootstrap support for that node. Methods of analysis are described in detail in Lamb (2021).

across paralogons 16 and 17, while the upper pair of chromosomes are common across paralogons 15 and 16. This contiguity is now known to have resulted from the fusion of three ancient chromosomes subsequent to 1R, but prior to 2R. Hence, for the paralogons shown in Fig. 9*A*, it can be concluded that the upper two rows diverged from the lower two rows at 1R, independent of molecular phylogenetic evidence. When all paralogons are considered, it is seen that nine fusions of chromosomes occurred between 1R and 2R, and analysis of those data provided confirmation of the 1R pairings for 12 of the paralogons (Lamb, 2021).

Emergence of distinct rod and cone isoforms. From analysis of paralogons and molecular phylogeny of the kind illustrated in Figs 8 and 9, it is possible to determine the pattern of gene duplications that gave rise to each of the rod *vs*. cone isoforms of phototransduction proteins, both prior to and during 2R-WGD. For the three key players in the activation steps of vertebrate phototransduction, Fig. 10 summarizes the occurrence of those duplications, relative to 2R-WGD. In each family, two ancient duplications occurred, prior to the divergence of tunicates and in some cases prior to the divergence of protostomes, that gave rise to the ancestral gene for each of a *GNAT*, a *PDE6* and a *CNGA* in the proto-vertebrate organism. Then, following the two rounds of genome duplication, it happens that each of those quadruplicated gene families lost one member and retained the other three.

By excluding from our present consideration those genes shown in green (whose protein products are expressed elsewhere than in rods and cones), we reach the important conclusion that the rod/cone duality of isoforms arose at the first round of genome duplication (1R) for each of the three illustrated gene families: *GNAT*s, *PDE6*s and *CNGA*s. Furthermore, though not shown here, it has been found that the rod/cone divergence of genes likewise occurred at 1R for the following additional four gene families: *PDE6G*/*PDE6H* (encoding the rod/cone PDE inhibitory subunits), *CNGB1*/*CNGB3* (encoding the rod/cone CNGC β-subunits), *SAG*/*ARR3* (encoding the rod/cone arrestins), and *SLC24A1*/*SLC24A2* (encoding the rod/cone NCKXs); see Lamb (2020), Fig. 22.

One important duplication occurred subsequent to 1R. For the *PDE6* family, it is clear that the rod-specific feature of a heterodimeric pair of isoforms, PDE6α and PDE6β (encoded by *PDE6A* and *PDE6B*), did not arise until the second round of genome duplication. Interestingly, this rod-specific distinction occurs only in jawed vertebrates, and not in jawless vertebrates (such as lampreys) where the rod-like photoreceptors utilize a homodimeric PDE6, just as cones do.

All jawed vertebrates use rhodopsin as the photopigment in their scotopic (rod) photoreceptors, yet it is unlikely that rhodopsin was the original scotopic photopigment. Instead, several lines of evidence indicate that the first scotopic opsin in proto-vertebrates was likely to have been pinopsin (Lamb, 2020; Sato et al., 2018), which arose prior to 1R when the gene for a C-opsin expressed in the retina duplicated to form pinopsin and a 'cone' opsin. Pinopsin's properties presumably enabled it to perform better than that other opsin under scotopic conditions, and it seems likely that from then onwards the two opsins were expressed in different cell types, specialized for scotopic and photopic conditions. Two

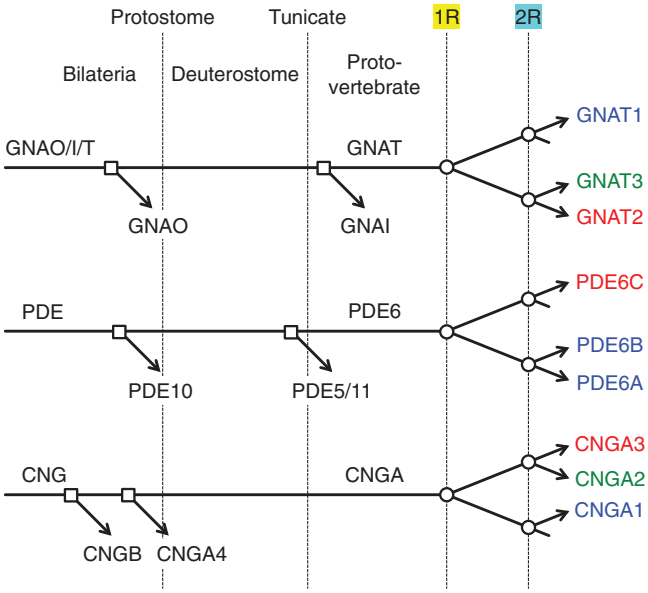

Figure 10. Summary of gene duplications underlying *GNAT*s, *PDE6*s and *CNGA*s
Deduced patterns and relative timing of gene duplications, for three proteins mediating activation steps in phototransduction. The horizontal axis is not to scale, but the four dotted vertical lines mark the following events. 'Protostome': the speciation divergence of protostomes from the deuterostome lineage; 'Tunicate': the speciation divergence of tunicates from the proto-vertebrate lineage; '1R' and '2R': the first and second rounds of whole-genome duplication. Squares (□) mark individual gene duplications; circles (○) mark whole-genome duplications. For the G-protein α-subunit, an ancestral gene duplicated in bilaterian times to give rise to a *GNAO* and a *GNAI*; then, around the time of the tunicate speciation, the *GNAI* underwent a tandem duplication to generate a *GNAI–GNAT* tandem pair. For the phosphodiesterase, an ancient duplication generated *PDE10* and *PDE5/11/6*, with the latter undergoing a duplication at around the time of the tunicate speciation, to generate the ancestral *PDE6*. For the cyclic nucleotide-gated channels, two ancient duplications generated a *CNGA* and a *CNGB*, with the former undergoing another ancient duplication to form the distinct *CNGA4* gene. Then, at 1R, each of *GNAT*, *PDE6* and *CNGA* duplicated and diverged, to give rise to separate rod- and cone-specific genes, shown in blue and red: *GNAT1* and *GNAT2*; *PDE6A/B* and *PDE6C*; and *CNGA1* and *CNGA3*. Green denotes isoforms used in cells other than rods or cones. Evidence in support of these branching patterns is presented in Lamb (2020).

other gene families also underwent gene duplications prior to 1R, the products of which may well have been of benefit to scotopic and photopic signalling: an ancestral *GRK* duplicated to form *GRK1* and *GRK7* (encoding the rod/cone receptor kinases), and several duplications occurred in the family of genes that encode GCAPs.

Accordingly, it seems likely that separate scotopic and photopic classes of retinal photoreceptor already existed in a proto-vertebrate organism prior to the first round of genome duplication. At least initially, both classes are likely to have resembled cones anatomically, though the scotopic class expressed pinopsin (and probably GRK1 and GCAP2), and would have exhibited slower and more sensitive responses suited for dim light. Then, following 1R, when rhodopsin emerged as a distinct gene, with properties even better suited than pinopsin to scotopic detection, it apparently became the opsin expressed in those scotopic photoreceptors. (To this day, a small proportion of rods in some jawed vertebrate species still express pinopsin instead of rhodopsin, Sato et al., 2018). At a later stage, though only in the jawed vertebrate lineage, those scotopic photoreceptors evolved to become 'true rods' with sealed-off discs and with the noise-resistant heterodimeric PDE6. In a process of parallel evolution in agnathans, their scotopic photoreceptors developed certain rod-like features (Asteriti et al., 2015; Morshedian & Fain, 2015, 2017), but they did not acquire fully sealed-off discs, and they retained the homodimeric PDE6 of cones; furthermore, a number of their other phototransduction genes may not be orthologous to jawed vertebrate rod genes (e.g. for the scotopic GRK and arrestin; see Figs 14 and 15 in Lamb, 2020).

Summary

The phototransduction cascade of vertebrate retinal photoreceptors is one of the best understood examples of G-protein-mediated signalling in sensory cells. Although the activation steps have been understood in quantitative terms for several decades, the recent discovery of a powerful non-linearity in the activation of the rod PDE6 has led to substantial revision of estimates for the magnitudes of the contributing gain parameters: in particular, it is now clear that a single activated molecule of rhodopsin activates transducin molecules at a rate exceeding 1000 G^*/s in mammalian rods; the mean lifetime of R^* activity is quite short, at around 70 ms, so that one R^* activates around 80 G^*s.

The principal difference in the transduction cascade in cone photoreceptors is the occurrence of much faster recovery, with the activated cone opsin shutting off in just a few milliseconds, and with the transducin/PDE6 shutting off within ∼10 ms, probably as a result of the greatly elevated expression of the RGS9 protein complex in cones. It is possible that the rate of transducin activation may be marginally lower in cones than in rods, but measurement is difficult.

Recent analysis of the shut-off reactions, taking account of the dimeric nature of the PDE6 in rods, along with the occurrence of a very low rate of aberrant terminations of R^* activity, has permitted a good description of the recovery kinetics of rod bright-flash responses. This model provides an accurate account of the form of the dominant time constant of recovery, measured as the slope of the relation between time spent in saturation and flash intensity plotted logarithmically.

It seems plausible that distinct photopic and scotopic photoreceptors evolved in a chordate ancestor of ours around 600 million years ago, and that the ancestral scotopic photoreceptors utilized pinopsin as their photopigment; in addition, the GRKs (G-protein receptor kinases) and the GCAPs may also have been distinct in those two classes of photoreceptor. However, it wasn't until the first round of whole-genome duplication (1R), around 550 Mya, that the opportunity arose to tailor each of the protein isoforms of those photopic and scotopic cells, so as to provide improved suitability to the differing needs of daytime and night-time vision. Thus, once there were duplicates of all the transduction genes, mutations and selection were able to fine-tune the properties of the proteins in the two classes of cell, which in due course became the cones and rods that are characteristic of all living jawed vertebrates. During the subsequent 500 My of evolution, there do not appear to have been major changes in molecular sequence of any phototransduction proteins, suggesting that cones and rods had already reached a very high level of performance by the time that the earliest jawed vertebrates evolved.

References

Asteriti, S., Grillner, S., & Cangiano, L. (2015). A Cambrian origin for vertebrate rods. *eLife*, **4**, e07166. https://doi.org/10.7554/eLife.07166.

Burns, M. E., & Lamb, T. D. (2003). Visual transduction by rod and cone photoreceptors. In *The visual neurosciences* (pp. 215–233). MIT Press.

Burns, M. E., & Pugh, E. N. (2010). Lessons from photoreceptors: Turning off G-protein signaling in living cells. *Physiology (Bethesda, Md)*, **25**, 72–84.

Calvert, P. D., Govardovskii, V. I., Krasnoperova, N., Anderson, R. E., Lem, J., & Makino, C. L. (2001). Membrane protein diffusion sets the speed of rod phototransduction. *Nature*, **411**(6833), 90–94.

Caruso, G., Bisegna, P., Lenoci, L., Andreucci, D., Gurevich, V. V., Hamm, H. E., & DiBenedetto, E. (2010). Kinetics of rhodopsin deactivation and its role in regulating recovery and reproducibility of rod photoresponse. *Plos Computational Biology*, **6**(12), e1001031.

Cowan, C. W., Fariss, R. N., Sokal, I., Palczewski, K., & Wensel, T. G. (1998). High expression levels in cones of RGS9, the predominant GTPase accelerating protein of rods. *Proceedings National Academy of Science USA*, **95**(9), 5351–5356.

Dobzhansky, T. (1973). Nothing in biology makes sense except in the light of evolution. *American Biology Teacher*, **35**(3), 125–129.

Dohrmann, M., & Wörheide, G. (2017). Dating early animal evolution using phylogenomic data. *Science Reports*, **7**(1), 3599.

dos Reis, M., Thawornwattana, Y., Angelis, K., Telford, M. J., Donoghue, P. C. J., & Yang, Z. (2015). Uncertainty in the timing of origin of animals and the limits of precision in molecular timescales. *Current Biology*, **25**(22), 2939–2950.

Friedburg, C., Thomas, M. M., & Lamb, T. D. (2001). Time course of the flash response of dark- and light-adapted human rod photoreceptors derived from the electroretinogram. *Journal of Physiology*, **534**(1), 217–242.

Gibson, S. K., Parkes, J. H., & Liebman, P. A. (2000). Phosphorylation modulates the affinity of light-activated rhodopsin for G protein and arrestin. *Biochemistry*, **39**(19), 5738–5749.

Gross, O. P., Pugh, E. N., & Burns, M. E. (2012). Calcium feedback to cGMP synthesis strongly attenuates single-photon responses driven by long rhodopsin lifetimes. *Neuron*, **76**(2), 370–382.

Hamer, R. D., Nicholas, S. C., Tranchina, D., Liebman, P. A., & Lamb, T. D. (2003). Multiple steps of phosphorylation of activated rhodopsin can account for the reproducibility of vertebrate rod single-photon responses. *Journal of General Physiology*, **122**(4), 419–444.

Heck, M., & Hofmann, K. P. (1993). G-protein-effector coupling: A real-time light-scattering assay for transducin-phosphodiesterase interaction. *Biochemistry*, **32**(32), 8220–8227.

Heck, M., Hofmann, K. P., Kraft, T. W., & Lamb, T. D. (2019). Phototransduction gain at the G-protein, transducin, and effector protein, phosphodiesterase-6, stages in retinal rods. *Proceedings National Academy of Science USA*, **116**(18), 8653–8654.

Kawamura, S., & Tachibanaki, S. (2008). Rod and cone photoreceptors: Molecular basis of the difference in their physiology. *Comparative Biochemistry and Physiology Part A: Molecular & Integrative Physiology*, **150**, 369–377.

Kumar, S., Stecher, G., Suleski, M., & Hedges, S. B. (2017). TimeTree: A resource for timelines, timetrees, and divergence times. *Molecular Biology and Evolution*, **34**(7), 1812–1819.

Lamb, T. D. (2010). Phototransduction: Adaptation in cones. In D. A. Dartt (ed.), *Encyclopedia of the eye* (Vol. **3**, pp. 354–360). Academic Press.

Lamb, T. D. (2020). Evolution of the genes mediating phototransduction in rod and cone photoreceptors. *Progress in Retinal and Eye Research*, **76**, 100823.

Lamb, T. D. (2021). Analysis of paralogons, origin of the vertebrate karyotype, and ancient chromosomes retained in extant species. *Genome Biology and Evolution*, **13**(4), evab044.

Lamb, T. D., & Kraft, T. W. (2016). Quantitative modeling of the molecular steps underlying shut-off of rhodopsin activity in rod phototransduction. *Molecular Vision*, **22**, 674–696.

Lamb, T. D., & Kraft, T. W. (2020). A quantitative account of mammalian rod phototransduction with PDE6 dimeric activation: Responses to bright flashes. *Open Biology*, **10**(1), 190241, https://doi.org/10.1098/rsob.190241.

Lamb, T. D., Patel, H., Chuah, A., Natoli, R. C., Davies, W. I. L., Hart, N. S., Collin, S. P., & Hunt, D. M. (2016). Evolution of vertebrate phototransduction: Cascade activation. *Molecular Biology and Evolution*, **33**(8), 2064–2087.

Lamb, T. D., & Pugh, E. N. (1992). A quantitative account of the activation steps involved in phototransduction in amphibian photoreceptors. *Journal of Physiology*, **449**(1), 719–758.

Leskov, I. B., Klenchin, V. A., Handy, J. W., Whitlock, G. G., Govardovskii, V. I., Bownds, M. D., Lamb, T. D., Pugh, E. N., & Arshavsky, V. Y. (2000). The gain of rod phototransduction: Reconciliation of biochemical and electrophysiological measurements. *Neuron*, **27**(3), 525–537.

Martemyanov, K. A., Krispel, C. M., Lishko, P. V., Burns, M. E., & Arshavsky, V. Y. (2008). Functional comparison of RGS9 splice isoforms in a living cell. *Proceedings National Academy of Science USA*, **105**(52), 20988–20993.

Morshedian, A., & Fain, G. L. (2015). Single-photon sensitivity of lamprey rods with cone-like outer segments. *Current Biology*, **25**(4), 484–487.

Morshedian, A., & Fain, G. L. (2017). The evolution of rod photoreceptors. *Philosophical Transactions of the Royal Society of London Series B: Biological Sciences*, **372**(1717), 20160074.

Nakatani, Y., Shingate, P., Ravi, V., Pillai, N. E., Prasad, A., McLysaght, A., & Venkatesh, B. (2021). Reconstruction of proto-vertebrate, proto-cyclostome and proto-gnathostome genomes provides new insights into early vertebrate evolution. *Nature Communications*, **12**(1), 4489.

Nikonov, S., Lamb, T. D., & Pugh, E. N. (2000). The role of steady phosphodiesterase activity in the kinetics and sensitivity of the light-adapted salamander rod photoresponse. *Journal of General Physiology*, **116**(6), 795–824.

Pentia, D. C., Hosier, S., & Cote, R. H. (2006). The glutamic acid-rich protein-2 (GARP2) is a high affinity rod photoreceptor phosphodiesterase (PDE6)-binding protein that modulates its catalytic properties. *Journal of Biological Chemistry*, **281**(9), 5500–5505.

Pugh, E. N., & Lamb, T. D. (1993). Amplification and kinetics of the activation steps in phototransduction. *Biochimica et Biophysica Acta*, **1141**(2–3), 111–149.

Qureshi, B. M., Behrmann, E., Schöneberg, J., Loerke, J., Bürger, J., Mielke, T., Giesebrecht, J., Noé, F., Lamb, T. D., Hofmann, K. P., Spahn, C. M. T., & Heck, M. (2018). It takes two transducins to activate the cGMP-phosphodiesterase 6 in retinal rods. *Open Biology*, **8**(8), 180075, https://doi.org/10.1098/rsob.180075.

Reingruber, J., & Holcman, D. (2008). The dynamics of phosphodiesterase activation in rods and cones. *Biophysical Journal*, **94**(6), 1954–1970.

Reingruber, J., Pahlberg, J., Woodruff, M. L., Sampath, A. P., Fain, G. L., & Holcman, D. (2013). Detection of single photons by toad and mouse rods. *Proceedings National Academy of Science USA*, **110**(48), 19378–19383.

Robson, J. G., & Frishman, L. J. (2014). The rod-driven a-wave of the dark-adapted mammalian electroretinogram. *Progress in Retinal and Eye Research*, **39**, 1–22.

Sacerdot, C., Louis, A., Bon, C., Berthelot, C., & Roest Crollius, H. (2018). Chromosome evolution at the origin of the ancestral vertebrate genome. *Genome Biology*, **19**(1), 166.

Sato, K., Yamashita, T., Kojima, K., Sakai, K., Matsutani, Y., Yanagawa, M., Yamano, Y., Wada, A., Iwabe, N., Ohuchi, H., & Shichida, Y. (2018). Pinopsin evolved as the ancestral dim-light visual opsin in vertebrates. *Communications Biology*, **1**(1), 156.

Simakov, O., Marlétaz, F., Yue, J.-X., O'Connell, B., Jenkins, J., Brandt, A., Calef, R., Tung, C.-H., Huang, T.-K., Schmutz, J., Satoh, N., Yu, J.-K., Putnam, N. H., Green, R. E., & Rokhsar, D. S. (2020). Deeply conserved synteny resolves early events in vertebrate evolution. *Nature Ecology & Evolution*, **4**(6), 820–830. https://doi.org/10.1038/s41559-020–1156-z.

Steinberg, R. H., Fisher, S. K., & Anderson, D. H. (1980). Disc morphogenesis in vertebrate photoreceptors. *Journal of Comparative Neurology*, **190**(3), 501–518.

Torre, V., Matthews, H. R., & Lamb, T. D. (1986). Role of calcium in regulating the cyclic GMP cascade of photo-transduction in retinal rods. *Proceedings National Academy of Science USA*, **83**(18), 7109–7113.

Vuong, T. M., Chabre, M., & Stryer, L. (1984). Millisecond activation of transducin in the cyclic nucleotide cascade of vision. *Nature*, **311**(5987), 659–661.

Yue, W. W. S., Silverman, D., Ren, X., Frederiksen, R., Sakai, K., Yamashita, T., Shichida, Y., Cornwall, M. C., Chen, J., & Yau, K.-W. (2019). Elementary response triggered by transducin in retinal rods. *Proceedings National Academy of Science USA*, **116**(11), 5144–5153.

Zhang, X., Wensel, T. G., & Kraft, T. W. (2003). GTPase regulators and photoresponses in cones of the eastern chipmunk. *Journal of Neuroscience*, **23**(4), 1287–1297.

Additional information

Competing interests

None declared.

Author contributions

Sole author.

Funding

None.

Acknowledgements

I am indebted to all my collaborators on the studies described in this review, and especially to E.N. Pugh Jr, T.W. Kraft, M. Heck, K.P. Hofmann, D.M. Hunt and H. Patel.

Open access publishing facilitated by Australian National University, as part of the Wiley – Australian National University agreement via the Council of Australian University Librarians.

Keywords

evolution, photoreceptor, phototransduction, retina, retinal cone, retinal rod

Supporting information

Additional supporting information can be found online in the Supporting Information section at the end of the HTML view of the article. Supporting information files available:

Peer Review History